JAAS

PAPER

View Article Online
View Journal | View Issue

Cite this: *J. Anal. At. Spectrom.*, 2025, **40**, 1049

Detection of Li in synthetic slags of Li-ion batteries by laser ablation inductively coupled plasma time of flight mass spectrometry (LA-ICP-ToF-MS)

Alena Schnickmann, *[a] Ciprian Stremtan,[b] Lukas Schlatt,[c] Thomas Schirmer[a] and Thomas Ulrich[a]

Lithium is one of the most important technological elements and is mainly used in Li-ion traction batteries (LIBs). Due to its high oxygen affinity, recovering this element from, *e.g.*, batteries is a challenge. In pyrometallurgical processes, Li accumulates in the slag and is currently largely lost. A new pyrometallurgical approach, called "engineered artificial minerals" (EnAM), deals with the modification of slag to enrich elements such as Li in a single phase with a simple chemical structure and favourable properties for processing (*e.g.* morphology). To maximise the efficiency of this process, the first step is to characterise as accurately as possible the distribution of the target element (here Li) across the phases in the slag. In this article, a combination of an electron-optical and X-ray based method (electron probe microanalysis) with a spatially resolved mass spectrometric method (laser ablation inductively coupled plasma time-of-flight mass spectrometry) is presented to study the distribution of Li in a synthetically produced slag. The combination of LA-ICP-ToF-MS multi elemental imaging with backscattered electron (BSE(Z)) imaging allows the resolution of intricate fine structures and the unambiguous identification of crystalline phases in the slag. Electron optics (backscattered electrons) provides high spatial resolution and mass spectrometry offers high sensitivity to detect Li. This makes it possible to characterise not only the stoichiometrically identifiable phases but also the non-stoichiometric amorphous components. By combining different analytical methods (toolbox), three Li-bearing phases could be clearly identified: the residual melt, Mn_3O_4 and $LiMnO_2$.

Received 13th September 2024
Accepted 27th January 2025

DOI: 10.1039/d4ja00334a

rsc.li/jaas

1 Introduction

In today's society, technological advancements are often accompanied by a shortage of elements such as Li, Ta or rare earth elements.[1] Reserves of these raw materials are limited,[2] and therefore an efficient long-term closed loop approach must be explored, especially to recover the critical elements from industrial waste streams. Efficient and economical recovery methods for Li are essential to secure the future and rapidly increasing demand for Li.

Li is often used in cathode materials for LIBs, where the initially primarily used $LiCoO_2$ is increasingly being replaced by Mn-bearing layered oxides ($LiNi_xMn_yCo_zO_2$ ($x + y + z = 1$; NMC))[3–5] or Li-manganates ($LiMnO_2$ and Li_2MnO_3)[6] for cost reasons. In order to recycle Li efficiently and completely, it is necessary to understand and verify how this element behaves during recycling processes. A promising approach for the recovery of Li is the recycling of spent LIBs.[7–10] During pyrometallurgical processing,[11] elements such as Li, Mg, Al and Mn enter the slag phase, while *e.g.*, Co, Ni, and Cu are recovered directly from the black mass as an alloy.[5,12,13] Consequently, Li can only be recovered by processing the slag in which Li should ideally be concentrated in a single phase during the slag formation process for efficient separation and reuse (EnAM approach). The Li-bearing phase could then be easily separated from the rest of the slag, *e.g.* by flotation[14,15] or magnetic separation.[16] At the same time, the incorporation of Li into other phases such as the matrix should be minimised or avoided completely (Fig. 1).

For the successful application of this Li recovery approach, the (fine)structure of the slag must first be analysed to clarify how Li behaves especially in the presence of redox-sensitive elements such as Mn, and what its distribution is after the crystallisation process in the sample. For this purpose, synthetic (syn.) slags, containing Li_2O, SiO_2, CaO and MnO as well as MgO and Al_2O_3 as trace elements have been prepared, which are comparable in composition to industrial slags. These syn. slags will be used to investigate the distribution of Li in the slag and what kind of Li-bearing phase(s) are formed. Based on

[a]*Department of Geoscience, Institute of Geotechnology and Mineral Resources, Clausthal University of Technology, Adolph-Roemer-Str. 2A, 38678 Clausthal-Zellerfeld, Germany. E-mail: alena.schnickmann@tu-clausthal.de*

[b]*Teledyne Photon Machines, 512 East Madison Avenue, Suite 4, Belgrade, MZ 59714, USA*

[c]*Nu Instruments, Unit 74, LL13 9XS Wrexham, UK*

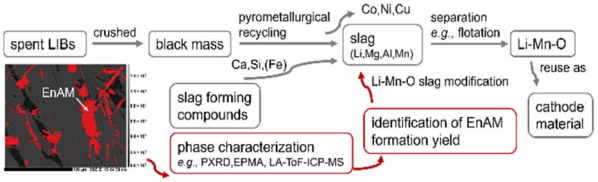

Fig. 1 Schematic illustration of the recycling path of used LIBs. The grey arrows show the industrial part. Our approach is shown in red. The aim of the synthetic slag preparation and characterization is to identify possible Li-rich phases and their formation regions for efficient Li recovery later in the industrial process.

these results, future slag production can be adjusted so that only one main Li-rich phase (EnAM) is formed that can be separated. Therefore, all Li-bearing phases (crystalline and amorphous) must first be characterised in detail (chemically and mineralogically) before the slag system and cooling curves can be modified to maximise the amount of Li bound in the EnAM compound.

For the bulk (Li) composition analysis of the slags produced, several analytical methods are available, including inductively coupled plasma atomic emission spectrometry (ICP-AES), ICP mass spectrometry (MS) or ICP optical emission spectrometry (OES). Mineralogical characterisation of the slag discussed in this article has already been carried out by Schnickmann *et al.*, *via* PXRD and EPMA, providing an overview of the number of phases and the (fine)structure.[17] Based on these results, $LiMnO_2$ was clearly identified, while the minor incorporation of Li into other phases (especially in the amorphous residual melt) could only be assumed. However, the difficulty remains in determining which other phases contain Li, especially for variable, difficult to calculate, non-stoichiometric phases. To investigate the exact spatial distribution of Li in individual phases a sensitive *in situ* technique is required. Various studies (*e.g.* ref. 18–28) have described and discussed the detection of Li and other elements by (nano) secondary mass spectrometry ((nano-) SIMS), laser ablation inductively coupled mass spectrometry (LA-ICP-MS), laser-induced breakdown spectroscopy (LIBS), X-ray photoelectron spectroscopy (XPS) and Auger electron spectroscopy (AES). However, the quantification of Li-concentrations using these methods still needs to be optimized. We have previously used XPS and AES to analyse Li in synthetic (syn.) slags, but both methods produced unsatisfactory results. The XPS instrument used (Kratos Axis Nova) typically measures areas of 300 × 700 μm. This area can be reduced to 15 × 15 μm if required. However, this reduces the number of photoelectrons emitted by the sample (larger area = better signal). In the case of the syn. slags studied, an area of 1200 × 1200 μm was measured in imaging mode, which did not provide any useful results. In the case of AES, two aspects were identified that led to poor results. First, the syn. slag was too highly charged, and second, the hemispherical detector used (Omicron Nano scanning Auger microscopy (SAM)) showed low transmission at low Auger energies, although NanoSAM is particularly suitable for small structures. At 0.0549 keV, the energy of Li(Kα) is almost in the ultraviolet range, which means that the energy of the Auger electrons is also very low. Accordingly, the detector system of the instrument used is currently unable to detect low-energy Auger electrons with sufficient sensitivity.

These preliminary investigations have shown that a method must be found to detect Li even in small crystalline grains (max. size < 10 μm) or in the matrix, as may occur in syn. slag. Due to the small circular beam size of 3 μm as well as the high spatial resolution, a series of experiments with LA-ICP-ToF-MS was carried out. The aim of this study was to qualitatively determine the Li distribution in fine-grained crystalline samples and to identify the phases in which Li has been incorporated by correlating LA-elemental distribution images and electron-optical images. The purpose of this correlation is to provide an accurate phase identification, and thus, an accurate documentation of the Li distribution. For this, we used a combination of three analytical methods:

(1) Powder X-ray diffraction (PXRD) provides a mineralogical overview of the crystalline phases.

(2) Electron probe microanalysis (EPMA) for major and minor element composition of the individual phases/grains (except for Li). Equally, thin section mapping, was applied to define regions of interest (ROIs) to be subsequently measured with LA-ICP-ToF-MS.

(3) LA-ICP-ToF-MS for qualitative LA elemental maps (including Li) that show the relative abundance and distribution of elements.

1.1 Background

Previous studies have shown that $LiAlO_2$ crystallises early in the slag and offers good EnAM properties, *i.e.*, a high Li content (10.35 wt% Li) and good separation properties (*e.g.*, flotation[14,29]).[30,31] Nevertheless, the incorporation of up to 3 wt% Si and its water solubility make this compound unattractive, particularly in hydrometallurgical applications. Moreover, in the presence of Mn, spinel and spinel solid solutions (especially Mn_3O_4 and $MnAl_2O_4$) form instead of $LiAlO_2$.[31]

Therefore, a new EnAM-approach considers the stabilization of a Li-manganate, in particular $LiMnO_2$ or Li_2MnO_3. These EnAM compounds would contain the strategically important element Mn in addition to the valuable element Li.[32] Another advantage would be the removal of Mn from the residual material/slag (*e.g.* when used as an additive in Portland cement). In addition, Li-manganates could be directly reused as a cathode material (in Li-manganese-dioxide (LMO) batteries). $LiMnO_2$ and Li_2MnO_3 both crystallise early in the slag and contain up to 11.88 wt% (Li_2MnO_3) and 7.39 wt% Li ($LiMnO_2$) in an ideally filled crystal. Furthermore, these phases contain virtually no Si.[17,33] Investigations by Schnickmann *et al.* show that an exchange of Li and Mn in the crystal lattice is possible within the Li-manganate structure, described using the following modified structural formulae of these phases: $Li_{(1-x)}Mn_{(1+0.33x)}O_2/Li_{(1+x)}Mn_{(1-0.33x)}O_2$ and $Li_{(2-x)}Mn_{(1+0.33x)}O_3/Li_{(2+x)}Mn_{(1-0.33x)}O_3$.[17]

Hausmannite ($Mn^{2+}Mn_2{}^{3+}O_4$) is another phase that often occurs together with Li-manganates such as $LiMnO_2$, and may

contain small amounts of Li.[34] Due to the variable spinel-like crystal structure of $Mn^{2+}Mn_2{}^{3+}O_4$, in which only some of the lattice positions (1/2 tetragonal and 1/8 octahedral) are occupied, additional lattice positions can also be filled if the charge balance is ensured and the ionic radius ratio to oxygen is comparable. One example is the additional incorporation of Li. This leads to a deviation from the ideal stoichiometric formula XY_2O_4, *e.g.* $Li_xMn_{1-(1/2)x}{}^{2+}Mn_2{}^{3+}O_4$ (modified after Paulsen and Dahn[34]). With regard to the radius of Li in tetragonal and octahedral coordination (0.59 Å *vs.* 0.76 Å (ref. 35)) compared to Mn^{2+} (tetrahedral, 0.66 Å (ref. 35)) and Mn^{3+} (octahedral, 0.65 Å (ref. 35)), the former incorporation mechanism is more plausible.

To promote the formation of this proposed EnAM (*e.g.* $LiMnO_2$), and hence, to prevent the incorporation of Li into other phases, the Li distribution in the slag must be obtained first. This information is important for the understanding of the behaviour of a highly volatile element such as Li during crystallisation processes and will be used to modify the system accordingly.

2 Experimental

2.1 Preparation of the synthetic slag

The precursor for the melt experiment was prepared by the gel combustion method, according to Blank *et al.*[36] and Ehi-Eromosele *et al.*,[37] to produce syn. slags as homogeneous as possible. The chemicals used and the method to produce syn. slag can be found in Schnickmann *et al.*[17]

2.2 Methods

The modal composition of the syn. slag sample is obtained using PXRD (Panalytical X-Pert Pro Diffractometer). A Co-X-ray tube (Malvern Panalytical GmbH, Kassel, Germany, $\lambda = 1.7902$ Å, 40 kV, 40 mA) was used and the diffractogram was recorded in a 2θ angle range from 5° to 100° (step size of 0.0066°; time per step of 150.45 seconds). The crystalline phases were identified using a combination of the American Mineralogist Crystal Structure Database[38] and the pdf-2 ICDD XRD Database.[39]

EPMA (Field Emission Cameca SXFIVE FE) was used to measure the major and minor element concentrations of individual crystals/grains and to define ROIs on polished thin sections. For the measurement (15 kV, beam size: 100–600 nm; Schottky type[40]) the Kα lines of Mg, Al, Si, Ca and Mn were used and the intensities of the characteristic X-rays were analysed using the X-PHI model.[41] The instrument was calibrated with certified reference materials (CRM: P&H Developments Ltd and Astimex Standards Ltd) and the accuracy of the instrument was determined by repeated measurements (N (total number of measurements) = 20) on the reference material rhodonite ($MnSiO_3$), to define the standard deviation [%] and detection limit [ppm] for each element: Mg 0.02%/113.3 ± 2.4, Al 0.004%/102.1 ± 3.8, Si 0.08%/159.8 ± 3.8, Ca 0.04%/111.2 ± 3.8 and Mn 0.05%/1098 ± 24.94.

While ICP-quadrupole of sector-field mass spectrometers could also be used, a LA-ICP-ToF-MS was employed for the multi-elemental imaging because of the high-resolution laser, the low detection limit, the high measurement accuracy due to the (near)-simultaneous measurement of the masses, and the high speed of data acquisition. A nanosecond ArF excimer laser (193 nm wavelength) (Iridia, Teledyne Photon Machines, Bozeman MT, USA) equipped with a water cooled MLase laser head capable of firing at a 1 kHz repetition rate and a cobalt ablation chamber was used for LA-ICP-ToF-MS multi elemental imaging.[42] The system was connected to a time of flight ICP-MS (Vitesse, NU Instruments, Wrexham, UK) into which the dry aerosol from the laser ablation cell was introduced *via* an Aerosol Rapid Introduction System (ARIS, Teledyne Photon Machines[43]). A cobalt cell was used in the long pulse configuration and a PEEK tubing with a 0.75 mm ID and 75 cm length was used as the sample transport tube to connect the two instruments.

Helium was used as carrier gas at a total flow of 0.75 LPM to which argon was added as make up gas (1.12 LPM) before entering the plasma (plasma power: 1300 W). 22 ml min^{-1} helium and 6 ml min^{-1} hydrogen were used to eliminate interferences using a segmented reaction cell in the ICP-MS. Optimization of the LA-ICP-ToF-MS setup was performed prior to the analysis using both NIST SRM612 and NIST SRM610 glass certified reference materials (National Institute for Standards and Technology, Gaithersburg MD, USA). Both laser and ICP-ToF-MS parameters were optimized for the highest sensitivity in the desired low mass range (5–60 amu), while keeping oxide formation as low as possible ($^{238}U^{16}O^+/^{238}U^+ \leq 2.5\%$) as well as laser induced fractionation, monitored by using the $^{238}U^+/^{232}Th^+$ ratio, close to 1. The speed of the system, observed as the single-pulse-response (SPR), and calculated as full width at 10% of the peak maximum, was also tuned and an SPR of 1.7 ms was achieved using a 3 μm circular beam (Fig. 2).

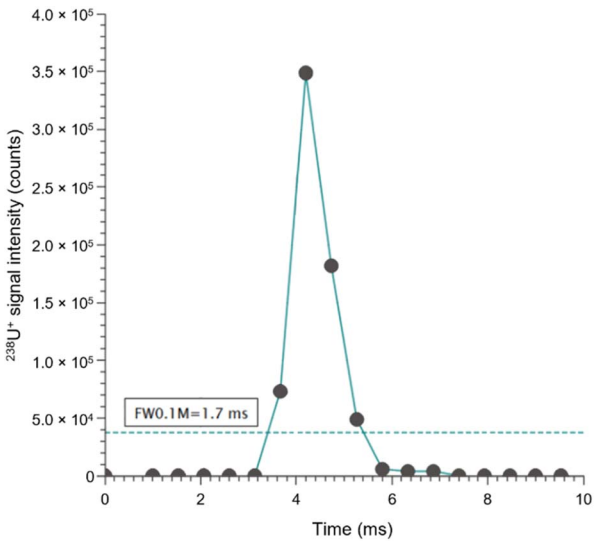

Fig. 2 Average peak profile for the transient $^{238}U^+$ signal of 2100 individual laser pulses fired on NIST SRM 612 using a spot size of 3 μm at a repetition rate of 300 Hz and a fluence of 3.5 J cm^{-2}. The blue dashed line marks the signal intensity at 10% of the maximum peak height (FW0.1M) and was used as the signal intensity threshold for calculating the single pulse response (SPR) of the system.

For the analysis, a mass range from 5 amu to 60 amu was acquired and 20 spectra were baseline subtracted, integrated and averaged before saving to disc every 0.26 ms. Due to a large interference of H_3O^+ of mass 19, this mass had to be removed. The elemental maps were acquired using the area scan tool, where the stages move at a constant speed across a designated area on the sample surface, while the laser fires at a fixed repetition rate. The stage scanning speed and laser repetition rate were optimized to minimize acquisition artifacts while maximizing the data acquisition rate. All experiments were carried out using a 3 μm circular beam, a fluence of 3.5 J cm^{-2}, a repetition rate of 1000 Hz and a dosage of 9, corresponding to 9 laser pulses per 3 μm pixel.[44,45]

Using a combination of the HDIP (Hierarchical Data Image Processor) software's automated image import and registration module, an overlay of the LA-elemental map and the BSE(Z) image can be created. This allows the element distribution to be directly assigned to different phases and the incorporation of light elements such as Li or trace elements into different phases to be examined in more detail. The transparency was adjusted using the Color Scheme Editor. It is also possible to further reduce the transparency in selected regions by using other image processing programs.

3 Results

A detailed mineralogical description and chemical bulk composition of the syn. slag have already been given by Schnickmann *et al.* and the main findings are briefly repeated here.[17]

3.1 ICP-OES – bulk composition

The ICP-OES analysis yields the bulk composition of the slag as 1.8 wt% Li, 1.2 wt% Mg, 1.1 wt% Al, 18.9 wt% Si, 29.0 wt% Ca, 8.6 wt% Mn and 39.4 wt% O.

3.2 PXRD – phase overview

PXRD results provide a first overview of the modal composition of the sample. The main components of the slag are the two matrix forming minerals $CaSiO_3$ (ICDD PDF2: 01-084-0654) and Ca_2SiO_4 (ICDD PDF2: 00-029-0369) as well as the Li-manganate $LiMnO_2$ (ICDD PDF2: 00-035-0749) (Fig. 3). Other phases could not be clearly identified due to line overlap. These results are used to support the interpretation of the LA-ICP-ToF-MS and EPMA results.

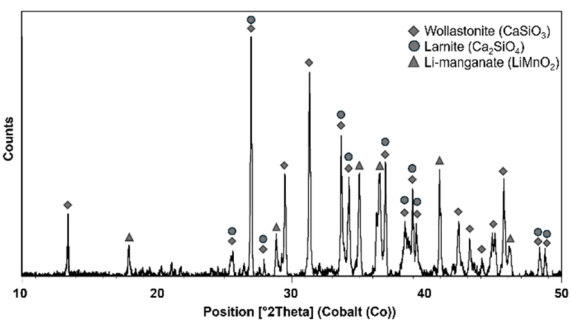

Fig. 3 Recorded PXRD pattern of slag samples. The identified main phases $CaSiO_3$, Ca_2SiO_4 and the Li-manganate $LiMnO_2$ are marked.

3.3 EPMA – elemental composition of individual phases

ROIs (Fig. 4) were defined and analysed by mapping the polished thin section of the representative slag using EPMA. To investigate the possible incorporation of Li into the different phases, these ROIs were subsequently analysed by LA-ICP-ToF-MS. The selected ROIs are shown in Fig. 4.

The *in situ* major element composition of the syn. slag was determined by WDX measurements. As shown by Schnickmann *et al.* and Schirmer *et al.* the Li content in stoichiometric phases can be calculated from the measured EPMA elemental concentration.[17,31] This calculation will not be discussed further as the focus of this manuscript is only on the qualitative Li distribution in the different phases.

The relationships between measured and calculated (*i.e.* Li) element concentrations in the respective phases, except for the Ca-silicates, are summarised in diagrams in Fig. 5a–d.

A total of 5 different phases were identified. In addition to the phases found with the PXRD analysis two different oxidic Mn-rich compounds can be distinguished. Based on their measured Mn content, these phases were assigned to $LiMnO_2$ and (Li-bearing) Mn_3O_4 (Fig. 4). There is a small deviation of the measured Mn concentrations in Mn_3O_4 from its ideal stoichiometric composition and it is suspected that this is due to the incorporation of Li into Mn_3O_4.[34] Based on the measured Mn concentrations, it was possible to document the exchange of Li and Mn in the crystal lattice of the Li-manganates, as well as the subordinate incorporation of Al, visible by the low scattering in Fig. 5a. A much larger scatter is seen in Fig. 5b, caused by a wide range of spinel solid solutions within the structure of

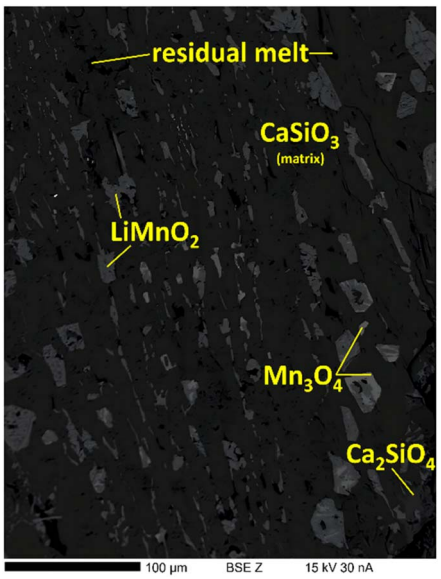

Fig. 4 BSE(Z) image of the investigated slag. Light gray: Mn_3O_4; medium gray: Li-manganate $LiMnO_2$; dark gray: the matrix forming phases $CaSiO_3$ and Ca_2SiO_4. The contrast was modified.

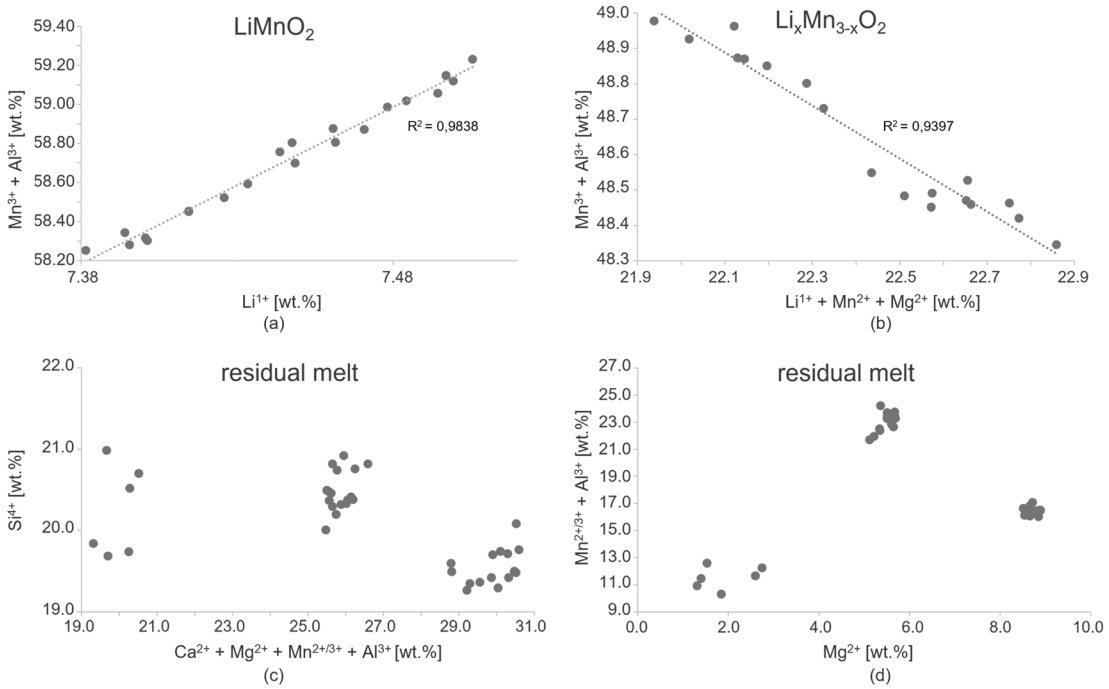

Fig. 5 Correlation diagrams based on the concentrations measured with EPMA in the crystals and the residual melt. The Li content was calculated *via* stoichiometric structure formulae and the measured concentrations of the other elements in the grain.[17,31] Calculation of Li in the residual melt is not possible (see text for explanation). (a) Relationship of Mn^{3+} (Ø 58.53 wt% ± 0.35) with Al^{3+} (Ø 0.35 wt% ± 0.04) and the calculated amount of Li (7.45 wt% ± 0.04) ($N = 20$), (b) occupation of tetrahedral sites – Li^{1+} (calculated; (Ø 0.51 wt% ± 0.17)), Mg^{2+} (Ø 0.71 wt% ± 0.19) and Mn^{2+} (Ø 24.01 ± 0.39), and octahedral sites – Al^{3+} (Ø 1.00 wt% ± 0.26) and Mn^{3+} (Ø 48.02 ± 0.39) in Mn_3O_4 ($N = 18$), and (c) and (d) elemental relations in the residual melt ($N = 38$), which consists of Mg (Ø 6.36 wt% ± 2.47), Al (Ø 1.03 wt% ± 2.32), Ca (Ø 0.92 wt% ± 0.56 Ca), Si (Ø 20.07 wt% ± 0.53) and Mn (Ø 18.24 wt% ± 4.31).

Mn_3O_4. Due to the highly variable composition of the residual melt, three distinct domains with slightly different element concentrations could be distinguished (Fig. 5c and d). The amorphous phase was unstable under the electron beam and resulted in fluctuations in the total element sums. In this phase, Li cannot be calculated like in stoichiometric phases due to variations in speciation of Mn (Mn^{2+}/Mn^{3+}) and is therefore not appearing in Fig. 5c and d.

3.4 LA-ICP-ToF-MS – identification of Li distribution

LA-ICP-ToF-MS is used to determine the spatial distribution of Li and to identify into which other phase(s) Li is incorporated apart from $LiMnO_2$.

For this, we created qualitative elemental maps of the previously defined ROIs and correlated these maps with the electron-optical images (in this case BSE images). The following nuclides were used for analysis: ^{7}Li, ^{24}Mg, ^{27}Al, ^{28}Si and ^{55}Mn. It can be seen that the elements Li and Mn are tightly correlated, which ultimately proves the formation of the Li–Mn-oxide $LiMnO_2$ (Fig. 6 and 7).

It is also possible to define grains/areas with less Li than the Li-manganates, which can be clearly distinguished as Li-bearing Mn_3O_4 (considering the measured Mn concentrations and the distinctly lighter grey colour in the BSE micrographs, Fig. 6a and f). The Li content in the matrix (*i.e.* eutectic residual melt) is very low as seen in the element distribution images (Fig. 6b and g).

Si is mainly incorporated into the Ca-silicates ($CaSiO_3$ and Ca_2SiO_4). Furthermore, high count rates of Si are detected in small clusters (Fig. 6d and i). In addition to Si, high Al counts were also observed in small clusters. The distribution of Al, which was only added to the slag as a trace element, is the most heterogeneous, with small amounts also incorporated into the Li-manganate and Li-bearing Mn_3O_4 (Fig. 6h), which has also been seen by EPMA. The residual melt contains all measured elements, including some Li. This was the first time that the incorporation of Li into the structure of Mn_3O_4 and the residual melt could be confirmed in a syn. slag.

To correlate the LA-elemental maps (expressed as relative abundances) with individual phases, a BSE(Z) image (Fig. 6e) of the syn. slag was superimposed (see the Methods). The transparency of the LA-elemental map was further reduced in selected regions to allow the determination of the exact phase in small grains/segregations/intergrowths (Fig. 7a–f). Furthermore, the false colour image with the blue coloured $LiMnO_2$ and the red coloured Li-bearing Mn_3O_4 also helps to differentiate the phases more easily (Fig. 7d). The intergrowth of Li-manganate and Li-rich Mn_3O_4 could be clearly distinguished (Fig. 7b and c).

It was noticed that areas of around 200 × 400 μm are ideal to overlay the LA-elemental maps. This allows even very small grains (<5 μm) to be categorized, and therefore, the respective phases to be clearly distinguished. In addition, the grain

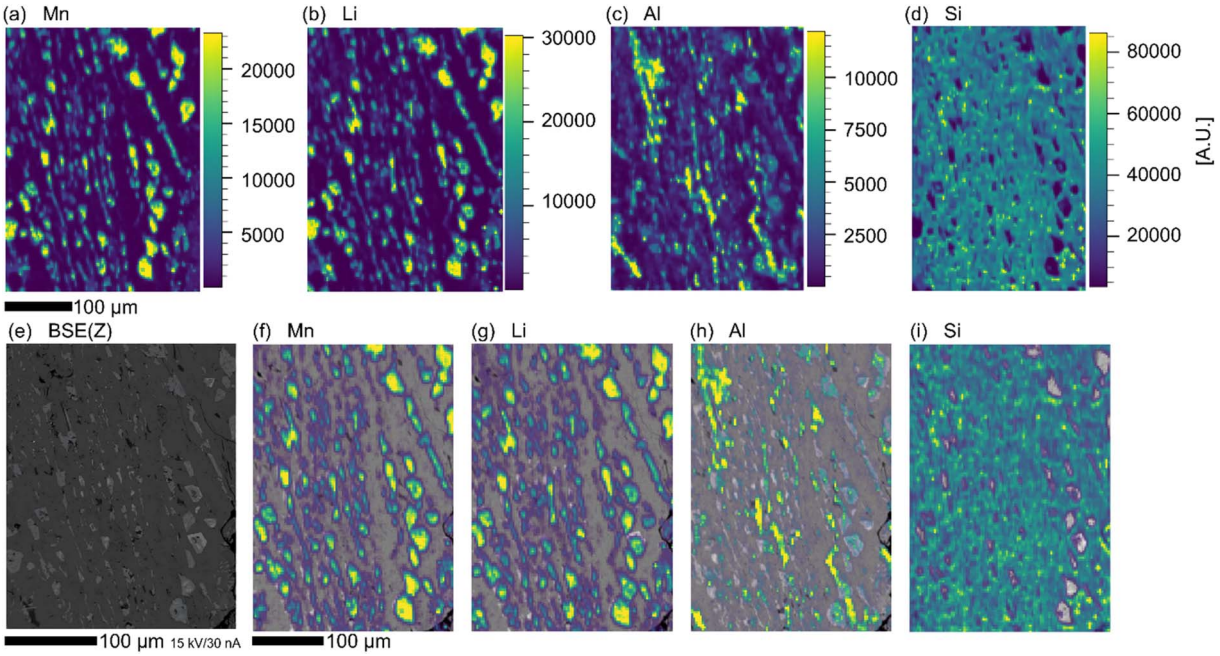

Fig. 6 Comparison of the LA-ICP-ToF-MS multi-elemental images with the BSE(Z) image. (a–d) Elemental distribution maps of the corresponding elements (relative intensities), (e) BSE(Z) image, and (f–i) overlaid LA-elemental map with the BSE(Z) image.

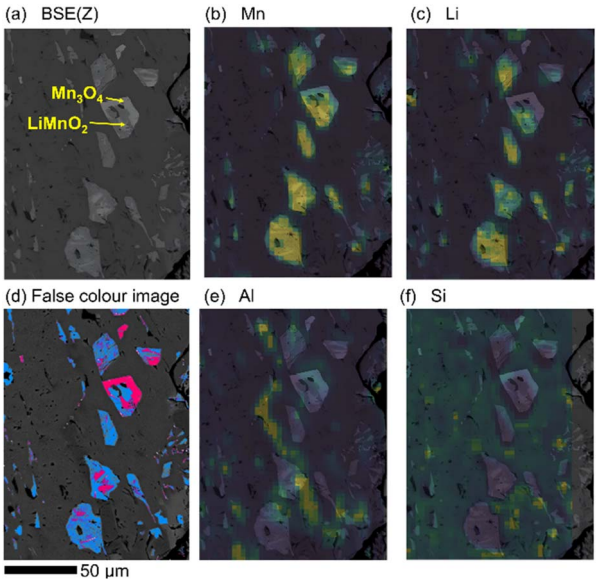

Fig. 7 Overlaid LA-elemental maps with the BSE(Z) image in a zoomed-in area. Transparency was further reduced to clearly differentiate between the phases. (a) BSE(Z) image of the region. (b) Combination of BSE(Z) image and LA-elemental map of Mn. (c) Combination of BSE(Z) image and LA-elemental map of Li. (d) BSE(Z) image with coloured grains, $LiMnO_2$ is coloured blue and Mn_3O_4 is coloured pink. (e) Combination of BSE(Z) image and LA-elemental map of Al. (f) Combination of BSE(Z) image and LA-elemental map of Si.

boundaries are distinctly visible. This distinguishes the different phases nicely within the ROI (Fig. 6f–i). For further investigations of even smaller features such as grain boundaries, smaller regions (*e.g.* 50 × 50 µm) could also be used.

The choice of the two methods EPMA and LA-ICP-Tof-MS to determine the distribution of Li in the slag was also due to the fine-grained texture of the slag. Generally, the grain sizes of the crystalline phases are very small, besides those of $CaSiO_3$. The crystal size of the idiomorphic to hypidiomorphic crystals of $LiMnO_2$ ranges between 60 and 157 µm, the subordinate hypidiomorphic to idiomorphic crystals of Mn_3O_4, which is often intergrown with $LiMnO_2$, up to a maximum of 34 µm, and the residual melt, which solidifies only at the end, between 37 and 246 µm.

4 Discussion

4.1 Toolbox for phase determination

In a Li-bearing multi-component system, a toolbox of different analytical methods is needed to ensure accurate and complete phase identification. In this study, particularly, the use of LA-ICP-ToF-MS shows promising results in the field of detection of Li in a complex slag system and the (fine) distribution of this element. These results are difficult to obtain with other spatially resolved methods due to limited spatial resolution, the relationship between beam size and signal intensity, or the limited range of elements that can be analysed with certain methods (*e.g.* EPMA and Li).

It has been shown that a combination of analytical techniques (toolbox) such as PXRD, EPMA and LA-ICP-(ToF)-MS is ideally suited to investigate the incorporation of Li into different phases in a complex and fine-gained material to achieve full phase analysis/characterisation because of the complementary information obtained from each method. The following procedures allowed the documentation of the relative Li distribution in the different phases:

(1) ICP-OES: bulk analysis of the sample, in this case, a synthetically produced slag. Identification of whether and how much total Li is present. This determines whether slag modification using the EnAM approach is feasible.

(2) PXRD: overview of the crystalline phases that have formed. Gives a first indication of possible solid solutions and what Li-manganate may have formed.

(3) EPMA: determination of the major element content in the individual crystals and in the melt, and definition of ROIs and phase identification based on phase-specific element contents. Recording of the BSE(Z) image for the observation of morphology and grain size, and for the correlation with the LA-elemental map.

(4) LA-ICP-(ToF)-MS: determination of the qualitative elemental distribution, including light elements such as Li. Subsequent correlation of the BSE(Z) image with the LA elemental map of regions no larger than 200 × 400 μm, with regions of 50 × 50 μm recommended for small structures such as grain boundaries. Correlation allows individual phases to be distinguished and the Li distribution to be studied in detail as well as the distribution of the other elements. Direct identification of the phases in which Li has been incorporated.

4.2 Li-distribution

Li is analysed qualitatively with LA-ICP-(ToF)-MS to visualize the distribution of this element in the syn. slag. The formation of Li–Mn oxides such as $LiMnO_2$ was clearly demonstrated for the first time, as was the incorporation of Li into the structure of Mn_3O_4 and the residual melt. These new findings confirm the previous assumptions (formation of $LiMnO_2$ and Li-containing Mn_3O_4) of Schnickmann *et al.*[17] From the result obtained, it can be assumed that only minute amounts of Li, if any, were incorporated into the matrix-forming phases $CaSiO_3$ or Ca_2SiO_4.

The main Li-scavanger is $LiMnO_2$, which is already being investigated as a cathode material,[4,46] and hence, turning out to be economically very interesting. The limited incorporation of impurities such as Al, as observed by LA-ICP-(ToF)-MS and EPMA, is not problematic because studies have already shown that small amounts of Al in the crystal lattice positively affect the efficiency of the battery due to improved Li transport.[47,48]

The morphology of the crystals indicates that the Li-manganate and Li-containing Mn_3O_4 formed first, followed by Ca-silicates ($CaSiO_3$ and Ca_2SiO_4) and then the residual melt, which probably solidified relatively quickly, filling small cavities. It is therefore suggested that a homogeneous melt was formed during the melting process, from which the phases crystallised during cooling.

The results obtained with the toolbox used indicate that slag modification is required to bind all the Li in a single compound such as $LiMnO_2$ that can be easily separated from the rest of the slag. The modification (*e.g.* adjustment of the cooling curves) should suppress the crystallisation of Mn_3O_4 and prevent Li from being left behind in the residual melt. Depending on the crystal structure of the produced Li-manganate, recrystallisation may be required prior to utilization as a cathode material. Accordingly, Li-manganates will be further investigated and characterized as potential new EnAMs in future studies.

5 Conclusions

In our study of Li-bearing syn. slags, we have tested a combination of complementing and relatively readily available analytical methods (PXRD, EPMA and LA-ICP-(ToF)-MS) to substitute for (nano)SIMS, AES, XPS and LIBS analysis. The latter methods have shortcomings in the analysis of, *e.g.*, Li-bearing phases in syn. slag due to their detection sensitivity (AES and XPS), spatial resolution (XPS and LIBS) or often matrix dependence ((nano)SIMS). In addition, compared to other methods ((nano)SIMS, XPS, and AES) LA-ICP-(ToF)-MS is easier to use/operate (*e.g.* no complex vacuum system or special sample preparation is required) and less expensive (*e.g.* compared to (nano)SIMS).

LA-ICP-(ToF)-MS shows very promising results in the field of Li detection in a multi-element slag system with fine-grained structures. For the first time, it was possible to directly differentiate between the Li-bearing phases in the syn. slags. The formation of $LiMnO_2$, as well as the incorporation of Li into the structure of Mn_3O_4 and the residual melt, could be demonstrated with certainty. It is still necessary to verify if a small amount of Li has been incorporated into the Ca-silicates. The next step will be to investigate the availability of matrix-matched Li-bearing standards to eventually quantify the results.

To ensure an accurate correlation between BSE(Z) images and LA-ICP-(ToF)-MS results without loss of information, an analysis area of 200 × 400 μm is suggested for overview and 50 × 50 μm for detailed images. In addition, it would be advantageous to maximise the crystal size of the Li-manganates in the future.

The LA-ICP-(ToF)-MS results provide an important contribution to the slag characterisation. Moreover, initial success has been achieved in correlating the LA-elemental map with electron-optical images. Based on the wide range of information obtained, slag production can be further adapted in the future so that all the Li is bound in a single phase (EnAM). Only by fully analysing and understanding the system, as we have done, can slag production be modified. This modification ensures that all the Li is incorporated into a phase that can be directly and easily separated, *e.g.* $LiMnO_2$.

Data availability

The data presented in this study are available upon request from the corresponding author.

Author contributions

Conceptualization, A. S.; methodology, A. S., C. S. and L. S.; validation, A. S., C. S. and L. S.; formal analysis, A. S.; investigation, A. S., C. S., L. S., T. S. and T. U.; data curation, A. S. C. S. and L. S.; writing—original draft preparation, A. S., T. S., C. S. and L. S.; writing—review and editing, A. S., C. S., L. S., T. S. and T. U.; visualization, A. S., C. S. and L. S.; supervision, T. S. and T.

U.; project administration, T. S. and T. U.; funding acquisition, T. S. All authors have read and agreed to the published version of the manuscript.

Conflicts of interest

The funders had no role in the design of the study; in the collection, analysis, or interpretation of the data; in the writing of the manuscript; or in the decision to publish the results.

Acknowledgements

This research was funded by the Open Access Publishing Fund of Clausthal University of Technology and the German Research Foundation within the framework of the Priority Programme: Engineered Artificial Minerals (EnAM) – a geometallurgical tool for the recovery of critical elements from waste streams (SPP 2315, Proj. No. 470309740). The LA-ICP-ToF-MS analysis was conducted at the Natural History Museum in London, and we would very much like to thank Dr Yannick Buret for giving us access to his laboratory.

References

1 European Commission, Directorate General for Internal Market, Industry, Entrepreneurship and SMEs, *Study on the EU's List of Critical Raw Materials (2020): Final Report., (LU)*, Publications Office, 2020, **https://data.europa.eu/doi/10.2873/11619**, accessed 20 December 2023.

2 U.S. Geological Survey, *Data Release for Mineral Commodity Summaries 2023*, U.S. Geological Survey Data Release, 2023.

3 N. Akhmetov, A. Manakhov and A. S. Al-Qasim, Li-Ion Battery Cathode Recycling: An Emerging Response to Growing Metal Demand and Accumulating Battery Waste, *Electronics*, 2023, **12**(5), 1152.

4 R. Saroha, A. Gupta and A. K. Panwar, Electrochemical Performances of Li-Rich Layered-Layered Li_2MnO_3-$LiMnO_2$ Solid Solutions as Cathode Material for Lithium-Ion Batteries, *J. Alloys Compd.*, 2017, **696**, 580–589.

5 L. Brückner, J. Frank and T. Elwert, Industrial Recycling of Lithium-Ion Batteries—A Critical Review of Metallurgical Process Routes, *Metals*, 2020, **10**(8), 1107.

6 F. Kong, R. C. Longo, M.-S. Park, J. Yoon, D.-H. Yeon, J.-H. Park, W.-H. Wang, S. Kc, S.-G. Doo and K. Cho, *Ab initio* study of doping effects on $LiMnO_2$ and Li_2MnO_3 cathode materials for Li-ion batteries, *J. Mater. Chem. A*, 2015, **3**, 8489–8500.

7 B. Makuza, Q. Tian, X. Guo, K. Chattopadhyay and D. Yu, Pyrometallurgical Options for Recycling Spent Lithium-Ion Batteries: A Comprehensive Review, *J. Power Sources*, 2021, **491**, 229622.

8 L. Reinhart, D. Vrucak, R. Woeste, H. Lucas, E. Rombach, B. Friedrich and P. Letmathe, Pyrometallurgical Recycling of Different Lithium-Ion Battery Cell Systems: Economic and Technical Analysis, *J. Cleaner Prod.*, 2023, **416**, 137834.

9 H. Bae and Y. Kim, Technologies of Lithium Recycling from Waste Lithium Ion Batteries: A Review, *Mater. Adv.*, 2021, **2**(10), 3234–3250.

10 Y. Ma and X. Du, Phase Transformations during the Oxidation of Fayalite in Iron-Rich Nickel Slag, *Int. J. Mater. Res.*, 2020, 290–296.

11 Z. J. Baum, R. E. Bird, X. Yu and J. Ma, Lithium-Ion Battery Recycling – Overview of Techniques and Trends, *ACS Energy Lett.*, 2022, **7**(2), 712–719.

12 M. Sommerfeld, C. Vonderstein, C. Dertmann, J. Klimko, D. Oráč, A. Miškufová, T. Havlík and B. Friedrich, A Combined Pyro- and Hydrometallurgical Approach to Recycle Pyrolyzed Lithium-Ion Battery Black Mass Part 1: Production of Lithium Concentrates in an Electric Arc Furnace, *Metals*, 2020, **10**(8), 1069.

13 X. Hu, E. Mousa, Y. Tian and G. Ye, Recovery of Co, Ni, Mn, and Li from Li-Ion Batteries by Smelting Reduction - Part I: A Laboratory-Scale Study, *J. Power Sources*, 2021, **483**, 228936.

14 A. Zgheib, S. Acker, M. H. Fischer, J. C. Namyslo, F. Strube, M. Rudolph, U. E. A. Fittschen, A. Wollmann, A. P. Weber, M. Nieger and A. Schmidt, Lithium Aluminate Flotation by pH- and Light-Switchable Collectors Based on the Natural Product Punicine, *RSC Adv.*, 2024, **14**(13), 9353–9364.

15 A. Vanderbruggen, J. Sygusch, M. Rudolph and R. Serna-Guerrero, A Contribution to Understanding the Flotation Behavior of Lithium Metal Oxides and Spheroidized Graphite for Lithium-Ion Battery Recycling, *Colloids Surf., A*, 2021, **626**, 127111.

16 A. Siddique, P. Boelens, F. Long, S. Zhou, V. Cnudde and T. Leißner, Characterization of Magnetic and Mineralogical Properties of Slag Particles from WEEE Processing, *Minerals*, 2023, **13**(11), 1417.

17 A. Schnickmann, S. Hampel, T. Schirmer and U. E. A. Fittschen, Formation of Lithium-Manganates in a Complex Slag System Consisting of Li_2O-MgO-Al_2O_3-SiO_2-CaO-MnO—A First Survey, *Metals*, 2023, **13**(12), 2006.

18 S. Müller, J. A. Meima and H.-E. Gäbler, Improving Spatially-Resolved Lithium Quantification in Drill Core Samples of Spodumene Pegmatite by Using Laser-Induced Breakdown Spectroscopy and Pixel-Matched Reference Areas, *J. Geochem. Explor.*, 2023, **250**, 107235.

19 R. Maeda, T. Van Acker, F. Vanhaecke, A. Yamaguchi, V. Debaille, P. Claeys and S. Goderis, Quantitative Elemental Mapping of Chondritic Meteorites Using Laser Ablation-Inductively Coupled Plasma-Time of Flight-Mass Spectrometry (LA-ICP-TOF-MS), *J. Anal. At. Spectrom.*, 2023, **38**(2), 369–381.

20 H. A. O. Wang and M. S. Krzemnicki, Multi-Element Analysis of Minerals Using Laser Ablation Inductively Coupled Plasma Time of Flight Mass Spectrometry and Geochemical Data Visualization Using t-Distributed Stochastic Neighbor Embedding: Case Study on Emeralds, *J. Anal. At. Spectrom.*, 2021, **36**(3), 518–527.

21 L. Ottolini and R. Oberti, Accurate Quantification of H, Li, Be, B, F, Ba, REE, Y, Th, and U in Complex Matrixes: A Combined Approach Based on SIMS and Single-Crystal Structure Refinement, *Anal. Chem.*, 2000, **72**(16), 3731–3738.

22 R. North, L. T. White, M. Nancarrow, A. Dosseto and D. Tanner, Sub-Micrometre Resolution FIB-SEM -based ToF-SIMS Used to Map Geochemical Zoning in Four Zircon

Reference Materials, *Geostand. Geoanal. Res.*, 2023, **47**(1), 125–142.

23 D. Gallot-Duval, C. Quéré, E. De Vito and J.-B. Sirven, Depth Profile Analysis and High-Resolution Surface Mapping of Lithium Isotopes in Solids Using Laser-Induced Breakdown Spectroscopy (LIBS), *Spectrochim. Acta, Part B*, 2024, **215**, 106920.

24 T. Schirmer, M. Wahl, W. Bock and M. Kopnarski, Determination of the Li Distribution in Synthetic Recycling Slag with SIMS, *Metals*, 2021, **11**(5), 825.

25 Y. Zhang, W. Zhai, X. Hu, Y. Jiang, S. Chen, Y. Zhang, W. Liu and Y. Yu, Application of Auger electron spectroscopy in lithium-ion conducting oxide solid electrolytes, *Nano Res.*, 2023, **16**, 4039–4048.

26 S.-K. Otto, Y. Moryson, T. Krauskopf, K. Peppler, J. Sann, J. Janek and A. Henss, In-Depth Characterization of Lithium-Metal Surfaces with XPS and ToF-SIMS: Toward Better Understanding of the Passivation Layer, *Chem. Mater.*, 2021, **33**, 859–867.

27 O. Breuer, Y. Gofer, Y. Elias, M. Fayena-Greenstein and D. Aurbach, Misuse of XPS in Analyzing Solid Polymer Electrolytes for Lithium Batteries, *J. Electrochem. Soc.*, 2024, **171**, DOI: 10.1149/1945-7111/ad2ef3.

28 S. Oswald, Auger- and X-ray Photoelectron Spectroscopy at Metallic Li Material: Chemical Shifts Related to Sample Preparation, Gas Atmosphere, and Ion and Electron Beam Effects, *Batteries*, 2022, **8**(24), DOI: 10.3390/batteries8030024.

29 S. Acker, J. C. Namyslo, M. Rudolph, F. Strube, U. E. A. Fittschen, H. Qiu, D. Goldmann and A. Schmidt, Polyether-Tethered Imidazole-2-Thiones, Imidazole-2-Selenones and Imidazolium Salts as Collectors for the Flotation of Lithium Aluminate and Spodumene, *RSC Adv.*, 2023, **13**(10), 6593–6605.

30 T. Elwert, K. Strauß, T. Schirmer and D. Goldmann, Phase Composition of High Lithium Slags from the Recycling of Lithium Ion Batteries, *World Metall.–Erzmet.*, 2012, **65**, 163–171.

31 T. Schirmer, H. Qiu, H. Li, D. Goldmann and M. Fischlschweiger, Li-Distribution in Compounds of the Li_2O-MgO-Al_2O_3-SiO_2-CaO System—A First Survey, *Metals*, 2020, **10**(12), 1633.

32 D. Kinch and E. Sadden, *EC Includes Copper and Manganese in Critical Minerals, Launches Strategic Minerals List*, 2023, https://www.spglobal.com/commodityinsights/en/market-insights/latest-news/metals/031623-ec-includes-copper-and-manganese-in-critical-minerals-launches-strategic-minerals-list, accessed 11 February 2024.

33 A. Schnickmann, D. A. De Abreu, O. Fabrichnaya and T. Schirmer, Stabilization of Mn_4^+ in Synthetic Slags and Identification of Important Slag Forming Phases, *Minerals*, 2024, **14**(4), 368.

34 J. M. Paulsen and J. R. Dahn, Phase Diagram of Li–Mn–O Spinel in Air, *Chem. Mater.*, 1999, **11**(11), 3065–3079.

35 R. D. Shannon, Revised Effective Ionic Radii and Systematic Studies of Interatomic Distances in Halides and Chalcogenides, *Acta Crystallogr., Sect. A*, 1976, **32**(5), 751–767.

36 D. H. A. Blank, H. Kruidhof and J. Flokstra, Preparation of $YBa_2Cu_3O_{7-\delta}$ by Citrate Synthesis and Pyrolysis, *J. Phys. D: Appl. Phys.*, 1988, **21**(1), 226–227.

37 C. O. Ehi-Eromosele, S. O. Ajayi and C. N. Onwucha, Influence of Fuels in the Sol-Gel Combustion Synthesis of Li_2MnO_3 Positive Electrode Material for Li-Ion Battery, *Mater. Chem. Phys.*, 2021, **259**, 124055.

38 R. T. Downs and M. Hall-Wallace, The American Mineralogist Crystal Structure Database, *Am. Mineral.*, 2003, **88**, 247–250.

39 S. Gates-Rector and T. Blanton, The Powder Diffraction File: A Quality Materials Characterization Database, *Powder Diffr.*, 2019, **34**(4), 352–360.

40 M. J. Jercinovic, M. L. Williams, J. Allaz and J. J. Donovan, Trace Analysis in EPMA, *IOP Conf. Ser.:Mater. Sci. Eng.*, 2012, **32**, 012012.

41 C. Merlet, Quantitative Electron Probe Microanalysis: New Accurate CI > (Pz) Description, *Electron Microbeam Analysis*, 1992, vol. 12, pp. 107–115.

42 S. J. M. Van Malderen, T. Van Acker and F. Vanhaecke, Sub-Micrometer Nanosecond LA-ICP-MS Imaging at Pixel Acquisition Rates above 250 Hz *via* a Low-Dispersion Setup, *Anal. Chem.*, 2020, **92**(8), 5756–5764.

43 T. Van Acker, S. J. M. Van Malderen, T. Van Helden, C. Stremtan, M. Šala, J. T. Van Elteren and F. Vanhaecke, Analytical Figures of Merit of a Low-Dispersion Aerosol Transport System for High-Throughput LA-ICP-MS Analysis, *J. Anal. At. Spectrom.*, 2021, **36**(6), 1201–1209.

44 M. Šala, V. S. Šelih, C. C. Stremtan, T. Tămaș and J. T. Van Elteren, Implications of Laser Shot Dosage on Image Quality in LA-ICP-QMS Imaging, *J. Anal. At. Spectrom.*, 2021, **36**(1), 75–79.

45 J. T. Van Elteren, M. Šala and D. Metarapi, Comparison of Single Pulse, Multiple Dosage, and 2D Oversampling/Deconvolution LA-ICPMS Strategies for Mapping of (Ultra) Low-Concentration Samples, *Talanta*, 2021, **235**, 122785.

46 R. C. Longo, F. T. Kong, S. Kc, M. S. Park, J. Yoon, D.-H. Yeon, J.-H. Park, S.-G. Doo and K. Cho, Phase Stability of Li–Mn–O Oxides as Cathode Materials for Li-Ion Batteries: Insights from *Ab Initio* Calculations, *Phys. Chem. Chem. Phys.*, 2014, **16**(23), 11233–11242.

47 F. Kong, R. C. Longo, M.-S. Park, J. Yoon, D.-H. Yeon, J.-H. Park, W.-H. Wang, S. Kc, S.-G. Doo and K. Cho, Ab Initio Study of Doping Effects on $LiMnO_2$ and Li_2MnO_3 Cathode Materials for Li-Ion Batteries, *J. Mater. Chem. A*, 2015, **3**(16), 8489–8500.

48 Y. Jang, Stability of the Monoclinic and Orthorhombic Phases of $LiMnO_2$ with Temperature, Oxygen Partial Pressure, and Al Doping, *Solid State Ionics*, 2000, **130**(1–2), 53–59.